48th AIAA Aerospace Sciences Meeting Including the New Horizons Forum and Aerospace Exposition
4 - 7 January 2010, Orlando, Florida

AIAA 2010-534

Numerical simulation and theoretical analysis on hypersonic boundary-layer receptivity to wall blowing-suction

Anatoli Tumin*
The University of Arizona, Tucson, AZ 85721, USA
Xiaowen Wang† and Xiaolin Zhong‡
The University of California, Los Angeles, CA 90095, USA

Direct numerical simulations on the receptivity of hypersonic boundary layers over a flat plate and a sharp wedge were carried out with two-dimensional periodic-in-time wall blowing-suction introduced into the flow through a slot. The free-stream Mach numbers are equal to 5.92 and 8 in the cases of adiabatic flat plate and sharp wedge, respectively. The perturbation flow field was decomposed into normal modes with the help of the multimode decomposition technique based on the spatial biorthogonal eigenfunction system. The decomposition allows for the filtering out of the stable and unstable modes hidden behind perturbations of another physical nature.

I. Introduction

The progress being made in computational fluid dynamics provides an opportunity for the reliable simulation of such complex phenomena as laminar-turbulent transition. The dynamics of flow transition depends on the instability of small perturbations excited by external sources. Computational results provide complete information about the flow field that would be impossible to measure in real experiments.

Recently, a method of normal mode decomposition was developed for two- and three-dimensional perturbations in compressible and incompressible boundary layers.[1–3] In Ref. 4, the method was applied to the theoretical analysis of the perturbation flow field in the vicinity of the blowing-suction actuator obtained from direct numerical simulation (DNS). The results demonstrated very good agreement between the amplitudes of the modes filtered out from the DNS data and those solved by linear theory of the flow receptivity to wall blowing-suction.

In the present work, we apply the multimode decomposition to DNS results downstream from the blowing-suction actuator in hypersonic boundary layers past a flat plate and a sharp wedge to compare the amplitudes of the modes found from the computations with the prediction of linear stability theory.

II. Outline of the multimode decomposition

The method of multimode decomposition of perturbations having a prescribed frequency is based on the biorthogonal eigenfunction system for linearized Navier-Stokes equations.[3] For the clarity of further discussion, we reproduce the main definitions necessary for discussing the present work.

We consider a compressible two-dimensional boundary layer in Cartesian coordinates, where x and z are the downstream and spanwise coordinates, respectively, and coordinate y corresponds to the distance from the wall. We write the linearized Navier-Stokes equations for a periodic-in-time perturbation (the frequency

*Professor, Department of Aerospace and Mechanical Engineering, Associate Fellow AIAA.
†Research Associate, Mechanical and Aerospace Engineering Department, Member AIAA.
‡Professor, Mechanical and Aerospace Engineering Department, Associate Fellow AIAA.

Copyright © 2010 by the authours. Published by the American Institute of Aeronautics and Astronautics, Inc., with permission.

is equal to zero in the case of a roughness-induced perturbation), $\sim \exp(-i\omega t)$, in matrix form as

$$\frac{\partial}{\partial y}\left(\mathbf{L}_0\frac{\partial \mathbf{A}}{\partial y}\right)+\mathbf{L}_1\frac{\partial \mathbf{A}}{\partial y}=\mathbf{H}_1\mathbf{A}+\mathbf{H}_2\frac{\partial \mathbf{A}}{\partial x}+\mathbf{H}_3\frac{\partial \mathbf{A}}{\partial z}+\mathbf{H}_4\mathbf{A}, \tag{1}$$

where vector $\mathbf{A}$ has 16 components

$$\begin{aligned}\mathbf{A}(x,y,z)=&(u,\partial u/\partial y,v,\pi,\theta,\partial\theta/\partial y,w,\partial w/\partial y,\partial u/\partial x,\partial v/\partial x,\\&\partial\theta/\partial x,\partial w/\partial x,\partial u/\partial z,\partial v/\partial z,\partial\theta/\partial z,\partial w/\partial z)^T.\end{aligned} \tag{2}$$

$\mathbf{L}_0,\mathbf{L}_1,\mathbf{H}_1,\mathbf{H}_2,\mathbf{H}_3$, and $\mathbf{H}_4$ are 16×16 matrices (their definitions are given in Ref. 5); u,v,w,π, and θ represent the three velocity components, pressure, and temperature perturbations, respectively; and the superscript T in (2) stands for the transpose. Matrix $\mathbf{H}_4$ originates from the nonparallel character of the flow. It includes terms with the y-component of the mean flow velocity and derivatives of the mean flow profiles with respect to the coordinate x.

In the quasi-parallel flow approximation, the solution of the linearized Navier-Stokes equations can be expanded into normal modes of the discrete and continuous spectra $\{\mathbf{A}_{\alpha\beta},\mathbf{B}_{\alpha\beta}\}$,[3] where $\mathbf{A}_{\alpha\beta}$ and $\mathbf{B}_{\alpha\beta}$ are eigenfunctions of the direct and adjoint problems, respectively. Subscripts α and β indicate the eigenfunctions corresponding to the streamwise, and spanwise wave numbers, respectively. The eigenfunction system $\{\mathbf{A}_{\alpha\beta},\mathbf{B}_{\alpha\beta}\}$ has an orthogonality relation given as

$$\langle \mathbf{H}_2\mathbf{A}_{\alpha\beta},\mathbf{B}_{\alpha'\beta}\rangle\equiv\int_0^\infty(\mathbf{H}_2\mathbf{A}_{\alpha\beta},\mathbf{B}_{\alpha'\beta})dy=\Gamma\Delta_{\alpha\alpha'}, \tag{3}$$

where Γ is a normalization constant, $\Delta_{\alpha\alpha'}$ is a Kronecker delta if either α or α' belongs to the discrete spectrum, and $\Delta_{\alpha\alpha'}$ is a Dirac delta function if both α and α' belong to the continuous spectrum.

In a weakly nonparallel flow, one can employ the method of multiple scales (MMS) by introducing fast (x) and slow ($X=\varepsilon x,\varepsilon\ll 1$) scales. The mean flow profiles depend on y and X only, whereas the perturbation will depend on both the fast and slow length scales. In the case of a discrete mode, the solution of the linearized Navier-Stokes equation is presented in the form

$$\mathbf{A}_\beta(x,X,y)=\left[D_\nu(X)\,\mathbf{A}^{(0)}_{\alpha_\nu\beta}(X,y)\,e^{i\int\alpha_\nu(X)dx}+\varepsilon\mathbf{A}^{(1)}_{\alpha_\nu\beta}(X,y)\,e^{i\int\alpha_\nu(X)dx}+\ldots\right], \tag{4}$$

where the function $D_\nu(X)$ has to be determined. After substituting Eq. (4) into Eq. (1), we arrive in $O(\varepsilon)$ at an inhomogeneous equation for $\mathbf{A}^{(1)}_{\alpha_\nu\beta}$. The solvability condition of this equation allows the finding of $D_\nu(X)$ (the details and relevant references are presented in Ref. 5).

III. Direct numerical simulation approach

In direct numerical simulation, the receptivity of hypersonic boundary layers over a flat plate and a sharp wedge to wall blowing-suction are considered by solving the two-dimensional compressible Navier-Stokes equations. Wall blowing-suction is introduced by an actuator located near the leading edge. In the assumption of thermally and calorically perfect flows, the governing equations in conservative variables are given as

$$\frac{\partial\vec{U}}{\partial t}+\frac{\partial}{\partial x}(\vec{F}_{1i}+\vec{F}_{1v})+\frac{\partial}{\partial y}(\vec{F}_{2i}+\vec{F}_{2v})=0, \tag{5}$$

where $\vec{U}$ is a column vector containing the conservative variables:

$$\vec{U}=\{\rho,\rho u,\rho v,e\}^T. \tag{6}$$

The flux vectors in (5) are divided into their inviscid and viscous components due to the fact that the two components are discretized with different schemes. The component $\vec{F}_{1i}$ and $\vec{F}_{2i}$, are inviscid flux whereas $\vec{F}_{1v}$ and $\vec{F}_{2v}$ are viscous flux components:

$$\vec{F}_{ji}=\begin{bmatrix}\rho u_j\\ \rho u u_j+p\Delta_{1j}\\ \rho v u_j+p\Delta_{2j}\\ u_j(e+p)\end{bmatrix}, \tag{7}$$

$$\vec{F}_{jv} = \begin{bmatrix} 0 \\ -\tau_{xx_j} \\ -\tau_{yx_j} \\ -\tau_{x_k x_j} u_k - K \frac{\partial T}{\partial x_j} \end{bmatrix}, \tag{8}$$

with $j, k \in (1, 2)$. In Cartesian coordinates, x_1 and u_1 are defined in the streamwise direction (x and u) whereas x_2 and u_2 are defined in the wall-normal direction (y and v).

Under the perfect gas assumption, pressure and energy are given by

$$p = \rho R T, \tag{9}$$

$$e = \rho c_v T + \frac{\rho}{2}(u^2 + v^2), \tag{10}$$

where c_v is the specific heat at constant volume. One can find details of the governing equations in Ref. 7.

In the present work, the fifth-order shock-fitting finite difference method of Zhong[8] is used to solve the governing equations in a domain bounded by the bow shock and the flat plate (or wedge). In other words, the bow shock is treated as a boundary of the computational domain. The Rankine-Hugoniot relations across the shock and a characteristic compatibility relation coming from downstream flow field are combined to solve for the flow variables behind the shock. The shock-fitting method makes it possible for the Navier-Stokes equations to be spatially discretized by high-order finite difference methods. Specifically, a fifth-order upwind scheme is applied to discretize the inviscid flux derivatives. By using the shock-fitting method, the interaction between the bow shock and the wall blowing-suction induced perturbations is solved as a part of solutions with the position and velocity of the shock front considered as dependent variables. The same numerical method was used in Refs. 10–12. Both cases correspond to the adiabatic wall boundary condition.

IV. Results

A. Flat plate

In the free-stream, the Mach number $M_\infty = 5.92$, temperature $T_\infty = 48.69$ K, and pressure $p_\infty = 742.76$ Pa. The Prandtl number and the specific heat ratio are 0.72 and 1.4, respectively. The dimensionless blowing-suction mass flux at the wall is expressed as

$$\begin{aligned} &(\rho v)' = \epsilon g(l) S(t), \qquad \epsilon = 0.405 \times 10^{-5}, \\ &g(l) = \begin{cases} 20.25 l^5 - 35.4375 l^4 + 15.1875 l^2, & (l \le 1); \\ -20.25 (2-l)^5 + 35.4375 (2-l)^4 - 15.1875 (2-l)^2, & (l > 1); \end{cases} \\ &l(x) = \frac{2(x - x_i)}{(x_e - x_i)}, \qquad x_i \le x \le x_e, \end{aligned} \tag{11}$$

where $x_i = 33$ mm and $x_e = 37$ mm are the coordinates of the leading and trailing edges of the slot, respectively. The amplitude distribution, $g(l)$, is shown in Fig. 1.

The function of time $S(t)$ in (11) is defined as

$$S(t) = \begin{cases} 1, & \mathrm{mod}(t, 20\mu s) \le 2\mu s; \\ 0, & \mathrm{mod}(t, 20\mu s) > 2\mu s. \end{cases} \tag{12}$$

The function $S(t)$ can be presented as a Fourier series.

Analyses of the mean flow velocity, temperature profiles and their derivatives have shown that they agree well with the self-similar solution for a boundary layer over a flat plate (see Appendix A). Only the second derivatives of the velocity and temperature profiles demonstrate some differences between the DNS results and the self-similar solution. A comparison of eigenvalues α obtained using the self-similar and DNS profiles is shown in Appendix B. There is a difference in α_i at high frequencies. In the analysis of the flat plate data, the self-similar profiles have been used in the stability equations. The analysis of the perturbations is limited

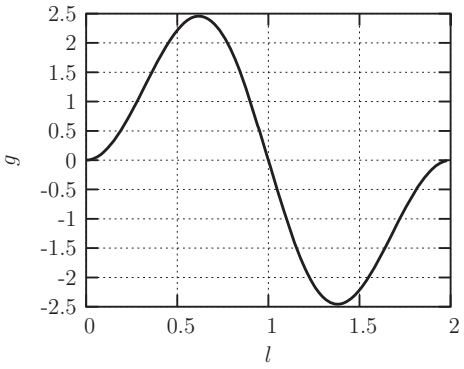

Figure 1. Amplitude distribution of the blowing-suction through the slot.

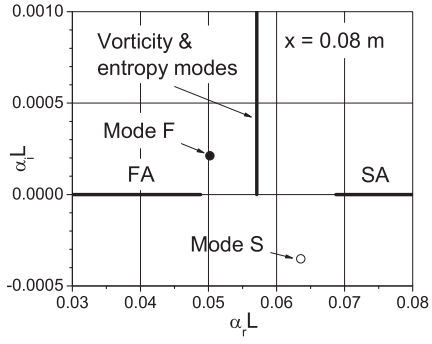

Figure 2. Discrete modes and the continuous spectrum.

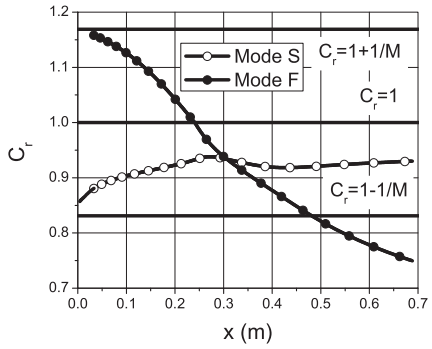

Figure 3. Real parts of the phase velocities of the discrete modes F and S scaled with the free-stream velocity U_∞.

to the DNS data corresponding to perturbations of 100 kHz only. In order to deal with the two-dimensional perturbations within the solver of Refs. 3, 5, the spanwise wave number β scaled with the Blasius length scale, $L = (\mu_\infty x/\rho_\infty U_\infty)^{1/2}$, was chosen to be equal to 10^{-5}.

In order to illustrate further analysis of DNS results, features of the spectrum should be introduced. Figure 2 shows the branches of the continuous spectrum and two discrete modes at $x = 0.08$ m. One of the discrete modes is labeled mode F (fast), the other is labeled mode S (slow). The mode names stem from their phase velocity features in the vicinity of the leading edge. One can see in Fig. 3 that mode S is synchronized with the slow acoustic wave ($c_r = 1 - 1/M_\infty$), whereas mode F is synchronized with the fast acoustic wave ($c_r = 1 + 1/M_\infty$). At the chosen flow parameters, mode F is always stable, and mode S is the unstable mode. One can see that mode F is synchronized with vorticity/entropy modes having dimensionless phase velocity $c_r = 1$ at $x \approx 0.25$ m. The significance of the decaying mode F stems from its synchronization with mode S, where the decaying mode can give rise to the unstable mode (switching of the modes), which may lead to the transition to turbulence.[13]

1. *Mode S*

Figure 4 shows the pressure perturbation on the wall (scaled with the free-stream pressure) obtained in the DNS and projections on the discrete mode S. Amplification of the discrete mode evaluated with and without the nonparallel flow effects (MMS and LST, respectively) is also presented in Fig. 4. One can see that the nonparallel flow effect is significant in this example. The DNS data for the wall pressure perturbation have wiggles near the actuator region due to input from the various modes present in the signal (Fig. 5). The filtered-out amplitude of the unstable mode S is smooth, and it is in good agreement with the theoretical prediction on the whole interval.

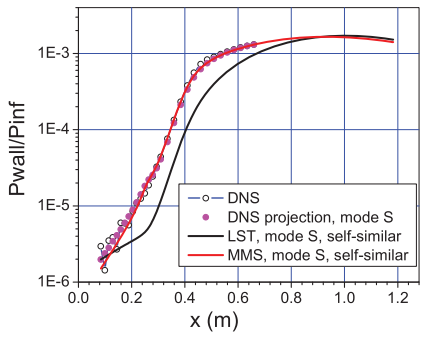

Figure 4. Projection of the DNS results onto the discrete mode S.

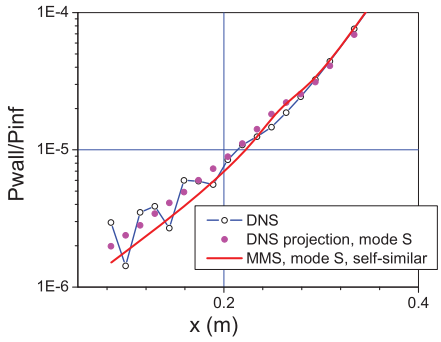

Figure 5. Closer view of the results in Fig. 4 in the vicinity of the actuator.

2. *Mode F*

It is interesting to look at the filtered-out decaying mode F on Fig 6. It is in good agreement with the theoretical prediction up to $x \approx 0.25$ m. After that, it experiences a jump and the amplitude becomes comparable with the amplitude of mode S. The result can be attributed to the next term in the expansion (4). The second term, $\mathbf{A}^{(1)}_{\alpha_\nu\beta}(X, y)$, can be expanded into an eigenfunction system. It is the standard problem of finding eigenfunctions of a perturbed operator using the unperturbed basis. For the non-resonance case when eigenvalues of modes F and S are distinct ($\alpha_S \neq \alpha_F$), it is straightforward to find a projection of $\mathbf{A}^{(1)}_{\alpha_S\beta}(X, y)$ onto $\mathbf{A}_{\alpha_F\beta}(X, y)$ (indices S and F indicate slow and fast discrete modes, respectively).

After the Fourier transform of the linearized equations (1) with respect to coordinate z and the substitution of $\mathbf{A}_\beta(x, X, y)$, one can derive the following equation for $\mathbf{A}^{(1)}_{\alpha_S\beta}(X, y)$:

$$\frac{\partial}{\partial y}\left(\mathbf{L}_0\frac{\partial \mathbf{A}^{(1)}_S}{\partial y}\right) + \mathbf{L}_1\frac{\partial \mathbf{A}^{(1)}_S}{\partial y} - \mathbf{H}_1\mathbf{A}^{(1)}_S - i\alpha_S\mathbf{H}_2\mathbf{A}^{(1)}_S - i\beta\mathbf{H}_3\mathbf{A}^{(1)}_S = \mathbf{\Phi}, \tag{13}$$

$$\mathbf{\Phi} \equiv \frac{dD_S(X)}{dX}\mathbf{H}_2\mathbf{A}^{(0)}_S + D_S(X)\,\mathbf{H}_2\frac{\partial \mathbf{A}^{(0)}_S}{\partial X} + D_S(X)\,\bar{\mathbf{H}}_4\mathbf{A}^{(0)}_S,$$

where $\bar{\mathbf{H}}_4 = \varepsilon^{-1}\mathbf{H}_4$. For the sake of brevity, we use subscript S to indicate the slow discrete mode having wave number α_S. One can represent the solution for $\mathbf{A}_S^{(1)}$ as an expansion into the eigenfunctions of the undisturbed operator. In symbolic form, we write

$$\mathbf{A}_S^{(1)} = \sum_{\alpha_k \neq \alpha_S} C_k(X)\mathbf{A}_k^{(0)}. \tag{14}$$

The symbolic form of the expansion (14) means that we include the expansion into the discrete modes and continuous spectrum as well. Assuming that there is no resonance ($\alpha_k \neq \alpha_S$), one can substitute $\mathbf{A}_S^{(1)}$ from Eq. (14) into Eq. (13). Using the dot product with the adjoint eigenvector $\mathbf{B}_F^{(0)}$, we arrive at the coefficient C_F:

$$C_F(X) = \frac{D_S(X)}{i(\alpha_F - \alpha_S)} \frac{\left\langle \mathbf{H}_2 \frac{\partial \mathbf{A}_S^{(0)}}{\partial X}, \mathbf{B}_F^{(0)} \right\rangle + \left\langle \bar{\mathbf{H}}_4 \mathbf{A}_S^{(0)}, \mathbf{B}_F^{(0)} \right\rangle}{\left\langle \mathbf{H}_2 \mathbf{A}_F^{(0)}, \mathbf{B}_F^{(0)} \right\rangle}. \tag{15}$$

The input of mode F into the second term of Eq. (4) has a wave number (and phase speed) corresponding to mode S. We call this contribution of mode F "S2F centaur" in order to emphasize the twofold character of the term. The wall pressure perturbation associated with "S2F centaur" is shown in Fig. 7. Although the theoretical result for mode F downstream from the point of synchronism demonstrates qualitatively the same behavior as the amplitude of the DNS projection onto mode F, there is a quantitative discrepancy that has yet to be understood.

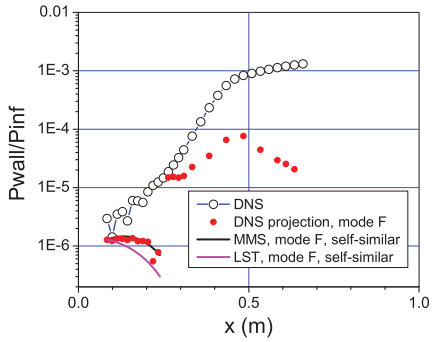

Figure 6. Projection of the DNS results onto the discrete mode F.

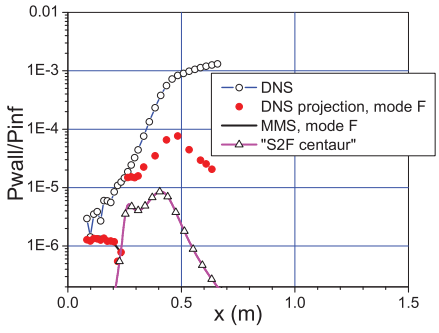

Figure 7. Projection of the DNS results onto the discrete mode F, and amplitude of "S2F centaur".

3. Velocity profiles of modes S and F

Having found the coefficients in the projection of the DNS results onto modes S and F, we can compare the velocity profiles of the modes with the DNS result in order to evaluate their significance at different distances from the actuator.

One can see that the main input into the velocity perturbation in the vicinity of the actuator is associated with the decaying discrete mode F. Far downstream, the unstable discrete mode S dominates the total signal.

B. Sharp wedge

In this example, periodic-in-time wall blowing-suction is introduced into the boundary layer over a wedge of half-angle 5.3 degrees. The free-stream Mach number $M_\infty = 8$, temperature $T_\infty = 54.8$ K, and pressure $p_\infty = 389$ Pa. The Prandtl number and the specific heat ratio are 0.72 and 1.4, respectively. The coordinates of the leading and trailing edges of the blowing-suction slot are $x_i = 51.84$ mm and $x_e = 63.84$ mm, respectively. These flow parameters and the actuator location correspond to the Case 3 considered in Ref. 4. The dimensionless wall blowing-suction mass flux at the wall is expressed as

$$(\rho v)' = q_0 g(l) \sum_{n=1}^{15} \sin(\omega_n t), \tag{16}$$

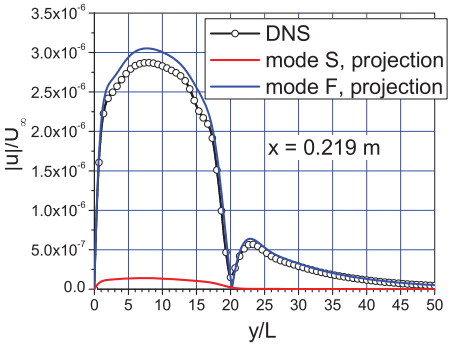

Figure 8. Streamwise velocity perturbation at $x = 0.219$ m.

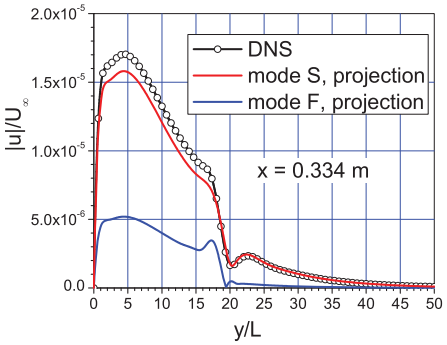

Figure 9. Streamwise velocity perturbation at $x = 0.334$ m.

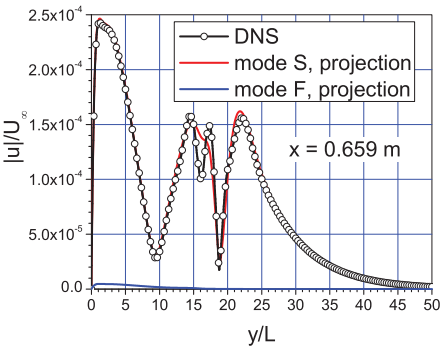

Figure 10. Streamwise velocity perturbation at $x = 0.659$ m.

where $q_0 = 0.734 \times 10^{-7}$ is a dimensionless amplitude parameter, scaled by the free-stream streamwise mass flux; the function $g(l)$ is defined in Eq. (11), and ω_n is the circular frequency of multi-frequency perturbations.

Figure 11 illustrates the pressure perturbations on the wedge at three frequencies: 44.76 kHz, 104.44 kHz, and 164.12 kHz.

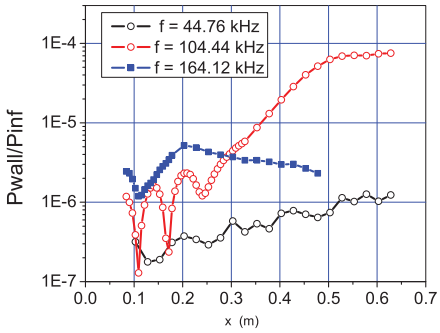

Figure 11. Pressure perturbations (p_{wall}/p_∞) on the wedge at three frequencies.

In the following examples, the analysis of the flow stability is based on the velocity and temperature profiles obtained from the computations without an assumption about the self-similar character of the boundary layer flow. In order to compare the projected amplitudes with those predicted using the method of multiple scales, we need derivatives with respect to x of the streamwise velocity and temperature profile of the mean flow. These derivatives were derived using the computational profiles together with the assumption that the profiles are locally self-similar.

Figure 12 shows the imaginary part of the wave number α scaled with $L = (\mu_\infty x/\rho_\infty U_\infty)^{1/2}$ obtained using the quasi-parallel approximation (LST) and using the method of multiple scales (MMS) for perturbations of frequency $f = 44.6$ kHz. Figure 13 shows wall pressure perturbations in DNS results and in their projection onto mode S together with the theoretical prediction made when nonparallel flow effects are included. Figures 14 and 15 show similar results corresponding to the frequency $f = 104.44$ kHz. Figures 16 and 17 demonstrate the results at frequency $f = 164.12$ kHz.

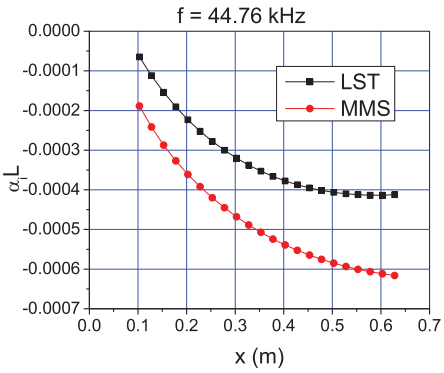

Figure 12. $Im(\alpha_i)$ versus x at frequency $f = 44.76$ kHz.

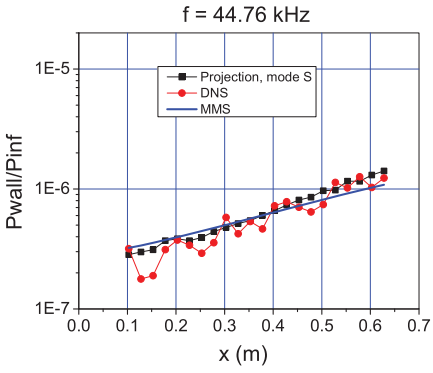

Figure 13. Projection of the DNS results onto the discrete mode S and comparison with the theoretical predictions using the method of multiple scales (MMS); $f = 44.76$ kHz.

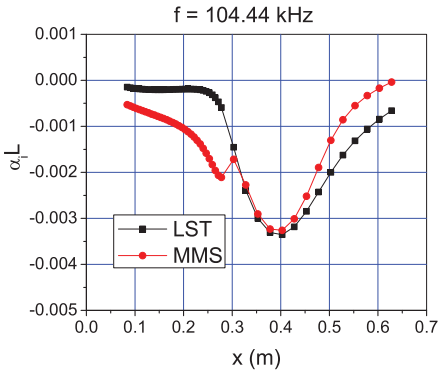

Figure 14. $Im(\alpha_i)$ **versus** x **at frequency** $f = 104.44$ **kHz.**

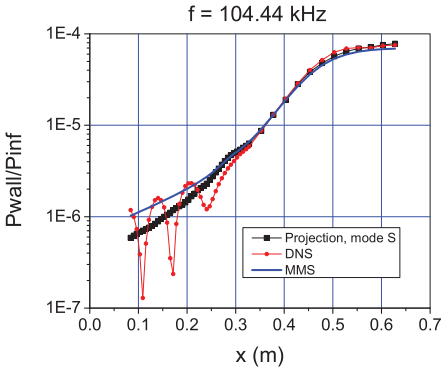

Figure 15. Projection of the DNS results onto the discrete mode S and comparison with the theoretical prediction using the method of multiple scales (MMS); $f = 104.44$ **kHz.**

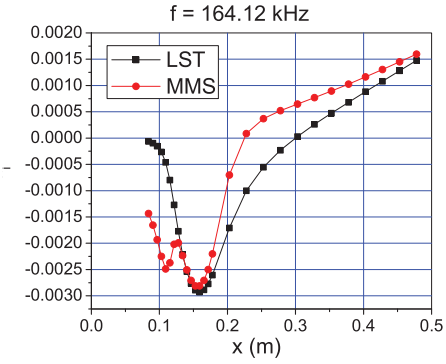

Figure 16. $Im(\alpha_i)$ **versus** x **at frequency** $f = 164.12$ **kHz.**

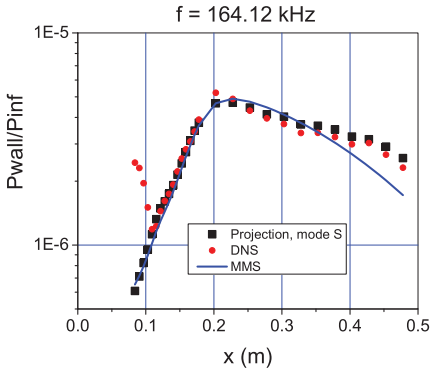

Figure 17. Projection of the DNS results onto the discrete mode S and comparison with the theoretical prediction using the method of multiple scales (MMS); $f = 164.12$ **kHz.**

V. Discussion of the results

The presented results illustrate how the multimode decomposition technique may serve as a tool for gaining insight into the flow dynamics in the presence of perturbations belonging to different modes. In the past, one could compare DNS results with theoretical prediction for unstable mode only far downstream from an actuator where the unstable mode dominates the total signal. Using the biorthogonal eigenfunction system, one can compare DNS results with theoretical predictions for unstable and stable modes in the vicinity of the actuator as well.

In Ref. 4 and in the present work, we have found that the multimode decomposition requires more elaborate analysis within the point of synchronism of mode F with the continuous spectra. Therefore, an extension of the theoretical model of Ref. 13 to the case of continuous spectrum is required.

A. Comparison of DNS mean velocity and temperature profiles with the self-similar solution

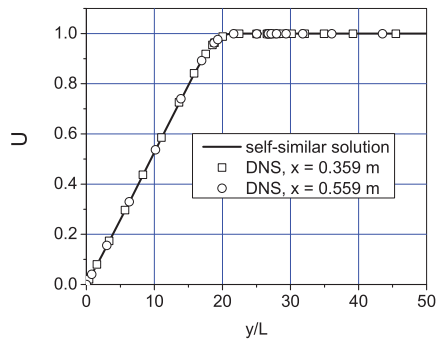

Figure 18. Self-similar solution (solid line) and DNS results (symbols) for the mean velocity profile $U(y)$.

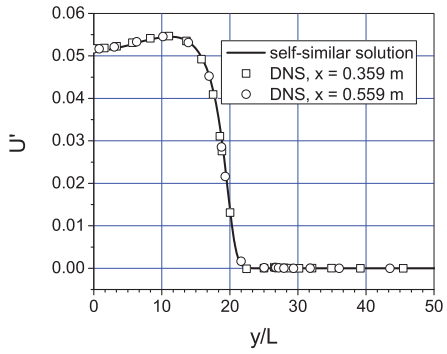

Figure 19. Derivative dU/dy: solid line - self-similar solution, symbols - DNS.

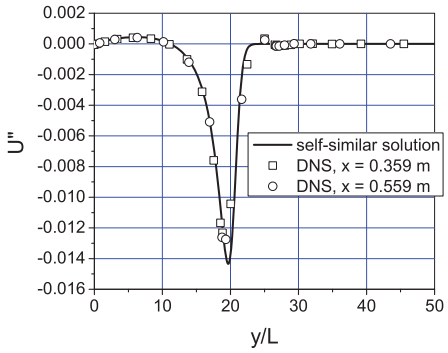

Figure 20. Derivative d^2U/dy^2: solid line - self-similar solution, symbols - DNS.

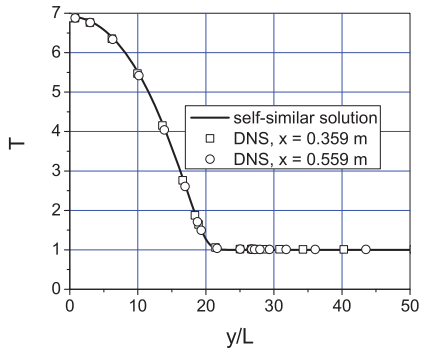

Figure 21. Mean temperature profile $T(y)$: solid line - self-similar solution, symbols - DNS.

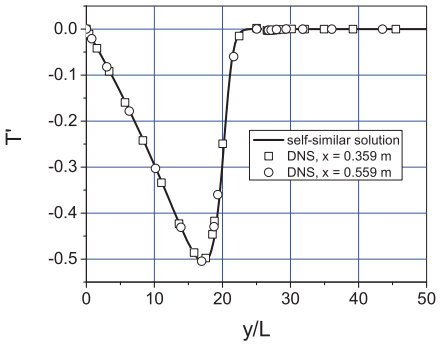

Figure 22. Derivative dT/dy: solid line - self-similar solution, symbols - DNS.

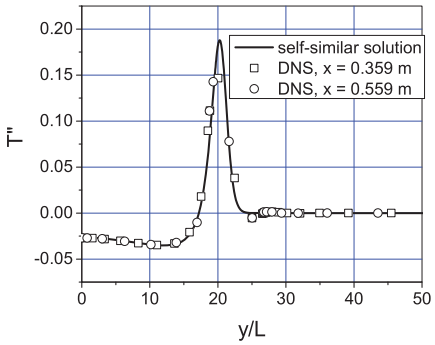

Figure 23. Derivative d^2T/dy^2: solid line - self-similar solution, symbols - DNS.

B. Comparison of eigenvalues $\alpha = \alpha_r + i\alpha_i$ obtained using DNS and self-similar profiles.

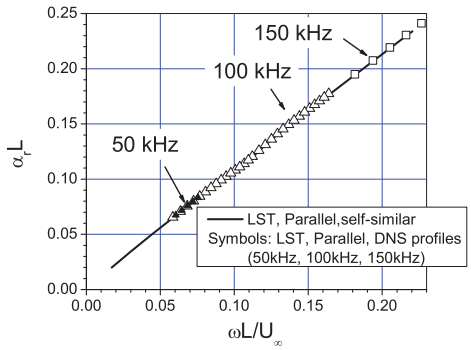

Figure 24. Comparison of α_r obtained using DNS and self-similar velocity and temperature profiles. Solid line - self-similar profiles; symbols - DNS profiles.

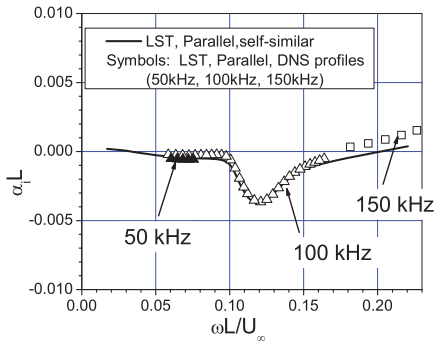

Figure 25. Comparison of α_i obtained using DNS and self-similar velocity and temperature profiles. Solid line - self-similar profiles; symbols - DNS profiles.

Acknowledgment

This work was sponsored by the AFOSR/NASA National Center for Hypersonic Research in Laminar-Turbulent Transition and by the Air Force Office of Scientific Research, USAF, under Grants No. FA9550-08-1-0322 (A.T.) and FA9550-07-1-0414 (X.Z. and X. W.) monitored by Dr. J. D. Schmisseur. The views and conclusions contained herein are those of the authors and should not be interpreted as necessarily representing the official polices or endorsements, either expressed or implied, of the Air Force Office of Scientific Research or the U. S. Government.

References

[1]Tumin, A., "Multimode decomposition of spatially growing perturbations in a two-dimensional boundary layer," *Phys. Fluids*, Vol. 15, 2003, pp. 2525–2540.

[2]Gaydos, P. and Tumin, A., "Multimode decomposition in compressible boundary layers," *AIAA J.*, Vol. 42, 2004, pp. 1115–1121.

[3]Tumin, A., "Three-dimensional spatial normal modes in compressible boundary layers," *J. Fluid Mech.*, Vol. 586, 2007, pp. 295–322.

[4]Tumin, A., Wang, X., and Zhong, X., "Direct numerical simulation and the theory of receptivity in a hypersonic boundary

layer," *Phys. Fluids*, Vol. 19, No. 1, 2007, paper 014101.

[5]Tumin, A., "Nonparallel flow effects on roughness-induced perturbations in boundary layers," *J. Spacecraft and Rockets*, Vol. 45, No. 1, 2008, pp. 1176–1184.

[6]Wang, X. and Zhong, X., "Receptivity of a Mach 8.0 flow over a sharp wedge with half-angle 5.3° to wall blowing-suction," AIAA Paper 2005–5025, 2005.

[7]Wang, X. and Zhong, X., "Effect of wall perturbations on the receptivity of a hypersonic boundary layer," *Phys. Fluids*, Vol. 21, 2009, Paper 044101.

[8]Zhong, X., "High-Order Finite-Difference Schemes for Numerical Simulation of Hypersonic Boundary-Layer Transition," *Journal of Computational Physics*, Vol. 144, 1998, pp. 662–709.

[9]Zhong, X. and Lee, T., "Nonequilibrium real-gas effects on disturbance/bow shock interaction in hypersonic flow past a cylinder," AIAA Paper 1996-1856, 1996.

[10]Ma, Y. and Zhong, X., "Receptivity of a supersonic boundary layer over a flat plate. Part 1: Wave structures and interactions," *J. Fluid Mech.*, Vol. 488, 2003, pp. 31–78.

[11]Ma, Y. and Zhong, X., "Receptivity of a supersonic boundary layer over a flat plate. Part 2: Receptivity to freestream sound," *J. Fluid Mech.*, Vol. 488, 2003, pp. 79–121.

[12]Ma, Y. and Zhong, X., "Receptivity of a supersonic boundary layer over a flat plate. Part 3: Effects of different types of free-stream disturbances," *J. Fluid Mech.*, Vol. 532, 2005, pp. 63–109.

[13]Fedorov, A. V. and Khokhlov, A. P., "Prehistory of instability in a hypersonic boundary layer," *Theor. Comp. Fluid Dyn.*, Vol. 14, 2001, pp. 359–375.